

## Article

# Umbrella Sampling Simulations of Carbon Nanoparticles Crossing Immiscible Solvents

Anastasios Gotzias 

National Centre for Scientific Research “Demokritos”, Institute of Nanoscience and Nanotechnology INN, 15310 Athens, Greece; a.gotzias@inn.demokritos.gr; Tel.: +30-210-650-3408

**Abstract:** We use molecular dynamics to compute the free energy of carbon nanoparticles crossing a hydrophobic–hydrophilic interface. The simulations are performed on a biphasic system consisting of immiscible solvents (i.e., cyclohexane and water). We solvate a carbon nanoparticle into the cyclohexane layer and use a pull force to drive the nanoparticle into water, passing over the interface. Next, we accumulate a series of umbrella sampling simulations along the path of the nanoparticle and compute the solvation free energy with respect to the two solvents. We apply the method on three carbon nanoparticles (i.e., a carbon nanocone, a nanotube, and a graphene nanosheet). In addition, we record the water-accessible surface area of the nanoparticles during the umbrella simulations. Although we detect complete wetting of the external surface of the nanoparticles, the internal surface of the nanotube becomes partially wet, whereas that of the nanocone remains dry. This is due to the nanoconfinement of the particular nanoparticles, which shields the hydrophobic interactions encountered inside the pores. We show that cyclohexane molecules remain attached on the concave surface of the nanotube or the nanocone without being disturbed by the water molecules entering the cavity.

**Keywords:** free energy; molecular dynamics; graphene; carbon nanocones



**Citation:** Gotzias, A. Umbrella Sampling Simulations of Carbon Nanoparticles Crossing Immiscible Solvents. *Molecules* **2022**, *27*, 956. <https://doi.org/10.3390/molecules27030956>

Academic Editors: Sylwester Furmaniak and Piotr A. Gauden

Received: 26 December 2021

Accepted: 28 January 2022

Published: 31 January 2022

**Publisher’s Note:** MDPI stays neutral with regard to jurisdictional claims in published maps and institutional affiliations.



**Copyright:** © 2022 by the author. Licensee MDPI, Basel, Switzerland. This article is an open access article distributed under the terms and conditions of the Creative Commons Attribution (CC BY) license (<https://creativecommons.org/licenses/by/4.0/>).

## 1. Introduction

Many of the pioneering simulations of surface phenomena involve studies of gases and liquids interacting with carbon solids [1–4]. Gas–solid or liquid–solid adsorption simulations allow assessing information about the micropore size, the surface area, and some aspects of the surface chemistry of sorbent materials [5–8]. Porous texture characterization based on gas adsorption is associated with a number of classical and advanced simulation tools performing at the microscopic level such as the density functional theory and Monte Carlo simulations [9–11]. On the other hand, the characterization of carbons with the help of liquids is especially interesting when the material is intended to be used in a liquid medium. Therefore, it makes sense to use liquids to characterize carbons when they are to be used for instance in liquid purification, liquid–solid heterogeneous catalysis, or liquid suspensions (and not to rely only, despite its popularity for the characterization by gas adsorption) [12,13].

When a carbon nanoparticle enters a solvent environment, the solvent molecules wash the surface and penetrate the accessible cavities. The molecules create a first layer covering the surface with either special composition and/or special interaction with the atomic sites and surface functional groups. Different solvents and solvent blends can be used upon treatment, for instance to deposit solute dopants on the surface of the nanoparticles [14]. The solvation energy is balanced by the fluid–wall interactions for fluids whose surface energy matches that of the walls [15,16]. Hence, hydrophobic carbons are more likely to dissolve in a hydrophobic environment than in a polar one.

Molecular dynamics can offer comprehensive microscopic insight to the solvation of particles by providing statistically sound views of interfacial structure and interaction potentials between solvents and solutes [17]. Most material frameworks bare different

chemical functions and may adopt a large number of conformations at the interface. Accordingly, a good knowledge of the surface chemistry and accessibility of the pore network are crucial to realize the affinities that contribute to the solvation process in different environments. It is with this motivation that we simulate the free energy of different carbon frameworks crossing hydrophobic–hydrophilic solvents [18,19]. Practicing with well-defined force fields (all-carbon solids, cyclohexane as the organic solvent, and SPC water) helps the formulation and execution of a sustainable workflow committed to free energy simulations [20–25]. The workflow is a precursor on an ongoing computational campaign investigating the binding affinities of such materials embedded in conjugated solvents with larger molecules such as polymers, surfactants, or lipids [26,27].

Due to its ability to assume different hybridization states, including  $sp$ ,  $sp^2$  and  $sp^3$  hybridization, carbon may form a miscellany of carbon allotropes with diverse physico-chemical characteristics and morphology [28,29]. If one excludes some specific cases such as diamond-like amorphous carbon, these allotropes are mainly constituted of covalently bonded  $sp^2$  carbons arranged in hexagonal atomic lattices. Typical carbon frameworks with exclusively  $sp^2$  hybridization are the fullerenes, the carbon nanotubes, and the graphene. These nanoparticles can be configured in single-layer or few-layer formations and therefore obtain a high specific surface area, which is essential for energy-storage applications. Due to their well-defined geometry, these nanoparticles can be used as starting materials for designing different nanoscale low-dimensional solids by controlling their dimensionality size and shape [30]. Given also their excellent electrical, mechanical, and thermal properties, they are regarded as emerging materials for sensors, semiconducting devices, and transparent electrodes. It is also impressive that these nanoparticles can potentially be exploited in high-priority biorelated fields. This has recently motivated research on the biocompatibility of the carbon interface and investigation of how carbons may replicate the affinity and transport properties of proteins [31–37].

A particular class of  $sp^2$  hybridized carbon nanoparticles that has received little attention is that of carbon nanocones (CNCs) [38–41]. CNCs were synthesised by accident in 1995 in the so-called Kvaerner Carbon Black and  $H_2$  process, which decomposes hydrocarbons directly into carbon and  $H_2$  [42]. Nowadays, conical carbon nanoparticles are produced through the pyrolysis of hydrocarbons in a plasma torch process [43]. CNCs moderately resemble open half fullerenes. The framework of the cones consists of regular hexagonal carbon rings and one to five pentagonal rings concentrated near the tip [44–46]. The cones occur in five different apex angles, depending on the number of the pentagons on the framework. Carbon nanocones as well as nanohorns (i.e., nanotubes capped with sharp cones at one end) have been proposed for a number of applications such as gas storage and heterogeneous catalysis and have been suggested as probes in electronic and optical nanoscale devices [47–52].

We build molecular models of three carbon nanoparticles, namely a carbon nanotube, a graphene sheet, and a carbon nanocone. We configure a biphasic system consisting of cyclohexane and water. We embed the carbon nanoparticle into the cyclohexane layer and push it to cross the interface and enter the water layer. We perform umbrella sampling simulations along the charted path of the nanoparticle and compute the solvation energy difference between the two solvents [53,54]. The water-accessible surface area of the nanoparticles along the path is also discussed. We demonstrate that cyclohexane remains adsorbed inside the confinement, protecting the hydrophobic carbon surface on the concave side from the more unfavorable interactions with the polar water molecules.

## 2. Materials and Methods

To generate the coordinate files of the graphene and the nanotube, we used the BuildCstruct python script [55,56]. We built a square graphene sheet with edge  $a = 3.0$  nm and an armchair nanotube, CNT(10,10) having a radius,  $r = 0.68$  nm and height,  $h = 4.5$  nm. We built the carbon nanocone by removing  $n_p = 3$  sectors of  $60^\circ$  from a flat graphene disc and connecting the dangling bonds. For each removed sector, we introduced one pentagon at the tip. The pentagons were topologically isolated, meaning that each pentagonal face

was surrounded by five hexagons. This gave an appropriate surface curvature near the apex of the cone. The cone angle,  $\theta$ , is given by the expression,  $\sin(\theta/2) = 1 - n_p/6$ . Setting  $n_p = 3$ , we obtained  $\theta = 60^\circ$ . The base radius of the cone was  $r = 2.09$  nm. Due to the apex curvature, the effective height of the cone was  $h_c = 3.55$  nm, that is, slightly smaller than the actual geometric height of the cone  $h_c = r/\tan(\theta/2) = 3.63$  nm. The modeling details of the carbon nanotube, the graphene, and the nanocone are listed in Table 1.

**Table 1.** Modeling parameters of the carbon nanotube, the graphene, and the nanocone and their external,  $S^{out}$ , and internal,  $S^{in}$ , surface areas. We used  $\sigma_C = 0.17$  nm in the geometrical surface area calculations.

Structure	Nanotube	Graphene	Nanocone
carbon atoms	760	416	1077
hydrogen atoms	40	58	57
edge, $\alpha$ , or base radius, $r$ (nm)	0.68	3	2.09
height, $h$ (nm)	4.5	3	3.55
geometrical surface, $S$ (nm <sup>2</sup> )	$S_{tube} = 2\pi r' h$	$S_{sheet} = 2\alpha h$	$S_{cone} = \pi r' (r' + \sqrt{h^2 + r'^2})$
$S^{out}(r' = r + \sigma_C)$	23.98	9.0	46.16
$S^{in}(r' = r - \sigma_C)$	14.36	-	36.13

We modeled the  $sp^2$  carbon atoms on the basis of the OPLSAA reference of naphthalene and of aliphatic carbons. Hydrogen atoms were modeled as benzene hydrogens. The carbon structures were uncharged. We used the GROMACS package, version 2020 to carry out the simulations. The simulations were submitted to the high-performance computing services of the Greek National Infrastructure for research and technology, GRNET-ARIS.

We placed the carbon nanoparticle at the center of a cubic simulation box with size  $l = 8$  nm. Selecting this size, we ensured that the nearest edge of the cube was distant more than 1.5 nm from the outermost carbon atom of the nanoparticle. The cut-off radius of the pair interactions was set to 1.4 nm. We used the *insert* command of GROMACS to insert 5500 cyclohexane molecules randomly into the  $l$ -cubic box. In all cases, less than 4500 molecules were successfully inserted. The  $CH_2$  nodes of the cyclohexane molecules were modeled as alkane carbons. We applied position restraints on the carbon nanoparticle and let the cyclohexane molecules relax using a steepest descent minimization followed by two equilibration steps, first in the NVT and then in the NPT ensemble over 0.2 and 1 ns, respectively. The pressure was regulated at 1 bar and the temperature was regulated at 310 K. Due to the pressure coupling, we expected the box to isotropically expand during the NPT equilibration, so that at the end of the simulations, the cube edge,  $l$ , became larger than 8 nm.

To build the biphasic system, we edited the box sizes to  $(X \times Y \times Z) = (l \times l \times 5/2 l)$ , where  $l$  is the cube size after the last NPT equilibration. In the output, the bottom  $l$ -cubic section of the box contained the equilibrated cyclohexane layer with the carbon nanoparticle at the center, while the upper  $l \times l \times 3/2 l$  section of the box was empty. The empty rectangular section was solvated with SPC water. In order to avoid placing water molecules into the cyclohexane layer, before triggering the *solvate* command of GROMACS, we changed the carbon (C) radius from 0.17 to 0.35 nm. For the rest of the simulation, the C radius was reset to 0.17 nm. As previously, the molecules of both solvents were relaxed, first using a steepest descent minimization, then an NVT equilibration over 0.5 ns and next an NPT over 1 ns. The pressure and the temperature were set to 1 bar and 310 K, respectively. After completing the equilibration steps, the box sizes and the number of the solvent molecules described therein are listed in Table 2.

**Table 2.** Box sizes after equilibration and the number of solvent molecules contained in the box with the carbon nanotube, the graphene, and the carbon nanocone.

Structure	Nanotube	Graphene	Nanocone
Volume $X \times Y \times Z$ (nm <sup>3</sup> )	$9.01 \times 9.01 \times 22.53$	$9.09 \times 9.09 \times 22.73$	$8.91 \times 8.91 \times 22.27$
cyclohexane molecules	4293	4338	4235
water molecules (spc)	34,235	35,410	32,702

To generate the initial configurations of the pertinent umbrella sampling simulations, we performed a pulling simulation. The pulling simulation continued from the last NPT equilibration. We removed the position restraints and pulled the carbon nanostructure along the  $z$  coordinate, using a force constant  $k = 1000 \text{ KJ mol}^{-1} \text{ nm}^{-2}$ . To specify the pulling direction, we drew a line connecting the COM of the carbon structure and a CH<sub>2</sub> node of a random cyclohexane molecule located above the structure (i.e., close to the interface, near the center of the box). Then, the pulling direction was given by the  $z$ -projection of the line. We used a pull rate  $10 \text{ nm ns}^{-1}$  and let the pulling simulation run over 1.5 ns. The carbon structure, the water molecules, and cyclohexane were indexed in different groups. The groups were coupled in separate temperature coupling paths. We applied the Nose–Hoover method for the temperature coupling and the Berendsen barostat for the pressure. The reference temperature and pressure were 310 K and 1 bar, respectively. We set the period of the temperature and pressure fluctuations to 1 picosecond. The timestep of the simulations was 1 fs.

The pulling simulation indicated a path through which the carbon nanoparticle traveled a distance, 10 nm (on the  $z$  axis), passing over the interface of cyclohexane and water. We used a default step size,  $dz = 0.23 \text{ nm}$ , to collect a number of configurations along the path. We collected additional configurations at the region of distances where the carbons laid close to the interface, using smaller step sizes such as  $dz = 0.11 \text{ nm}$  and  $dz = 0.06 \text{ nm}$ . The size and the number of the smaller steps depended on the width of the nanoparticle and the time it required to cross the interface. The selected configurations were given as inputs to the umbrella sampling simulations. The umbrella simulations started by running a brief, 0.2 ns, NPT equilibration step. The equilibrated configurations were passed into the long umbrella simulations (NPT), which ran over 10 ns. We used the Parrinello–Rahman pressure coupling to generate a rigorous NPT ensemble. Depending on the carbon nanoparticle, we performed a total of 45 to 60 umbrella simulations and generated a histogram of energy distributions (umbrella windows) throughout the charted path. We verified that the energy distributions were overlapping between any pair of consecutive ( $z, z + dz$ ) positions along the path. The umbrella simulations were submitted as an array of jobs and ran simultaneously on the computing nodes of GRNET. The computing performances of the umbrella simulations are listed in Table 3. After completing the simulations, we calculated the potential mean force (PMF) of the nanoparticles throughout the path, following the weighted histogram analysis method (WHAM) [57].

**Table 3.** Computing performance of the umbrella simulations (tasks) for the carbon nanotube, the graphene, and the nanocone, using 20 computer processor units (cpus) per task.

Structure	Nanotube	Graphene	Nanocone
ns/day	5.278	5.183	5.433
hours/ns	4.547	4.631	4.417

An interesting variable that can be continuously recorded during the course of the umbrella sampling simulations is the solvent-accessible surface area of the nanoparticles. This variable depicts how much of the surface is exposed to a particular solvent. We computed the solvent-accessible surface area using the double cubic lattice method of Eisenhaber et al. [? ]. The van der Waals radii of the atoms were taken from Bondi [59].

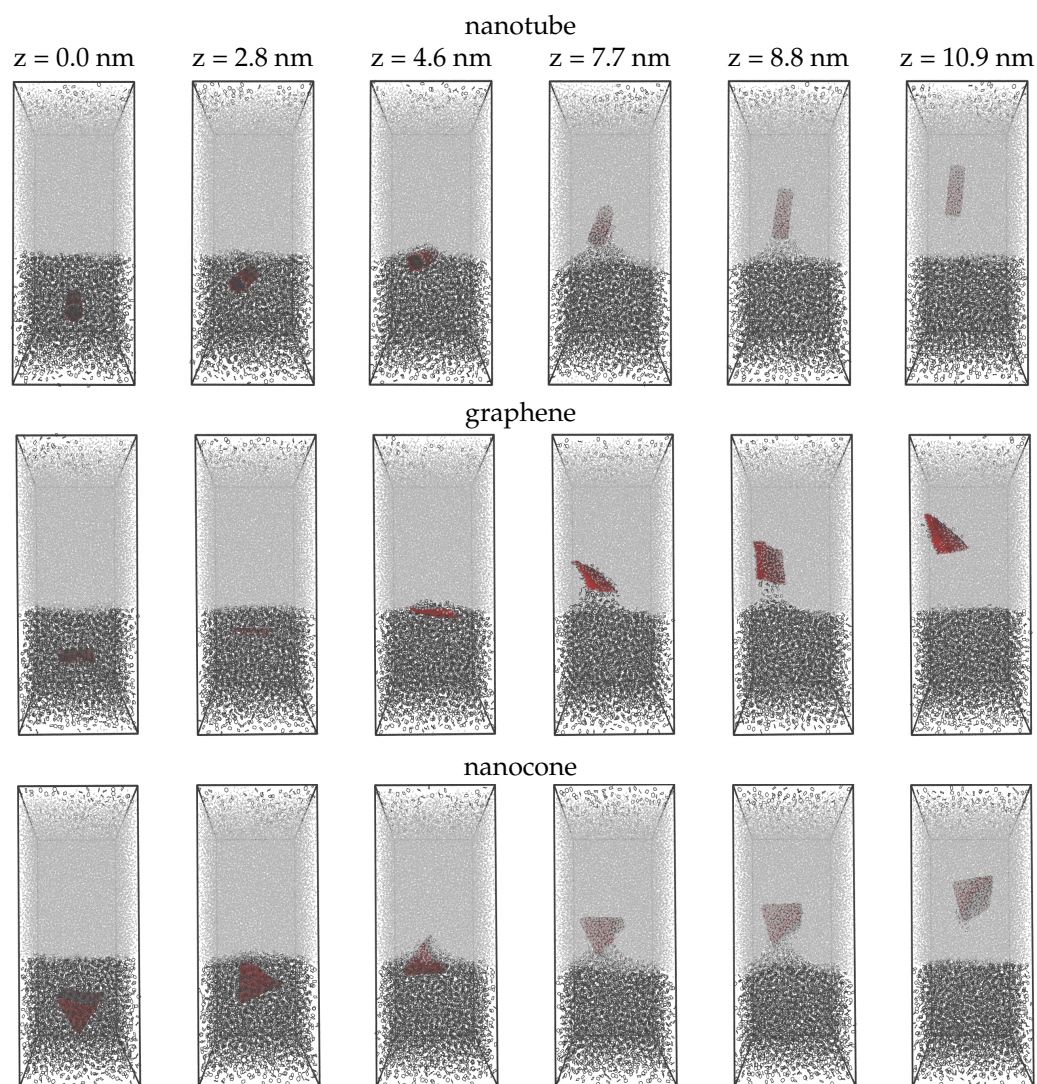


We grouped the non-water components of the system (i.e., cyclohexane molecules and the carbon particle) and set the carbon particle as the solute, for which we computed the surface area that was in contact with the different solvent (i.e., water).

### 3. Results

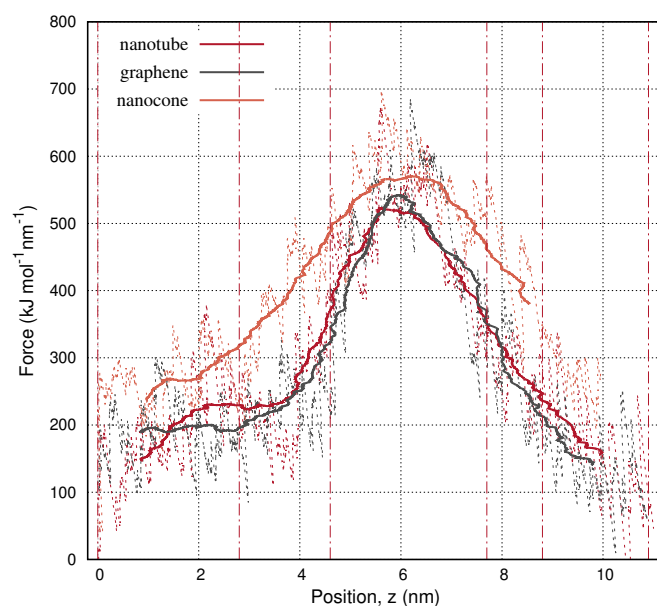
In Figure 1, we present a sequence of configurations from the pulling simulations performed on three carbon nanoparticles: namely, a nanotube, a graphene, and a nanocone. The box is solvated by two-fifths with cyclohexane and three-fifths with water. We apply a force to pull the carbon samples on the  $z$  direction. At  $z = 0$ , the samples lay at the center of the cyclohexane layer. The nanotube preserves an almost horizontal orientation up to the moment it crosses the interface. Within the water environment, the nanotube tends to align with the pulling coordinate, letting the cyclohexane molecules entrained by it drop back into the cyclohexane layer. Likewise, the graphene is initially planar to the interface. After crossing the interface, the graphene rotates nearly at a normal direction to align with the pulling coordinate. On the other hand, the nanocone obtains a clockwise motion as it moves on the  $z$  direction. When the nanocone enters the water environment, the tail shifts down, dropping some of the cyclohexane molecules carried inside the cavity. At the final configuration ( $z = 10.9$  nm), the carbon samples reach approximately a distance 5 nm from the interface. At this distance, the samples are totally dissolved in water as they do not interact with the cyclohexane molecules at the bottom layer. The interface of the solvents appears flat, while some of the stray cyclohexane molecules previously found in the water section have returned to the layer from which they originated. In all configurations, there is an amount of cyclohexane molecules located at the top of the water layer. This is an effect of the periodic boundary conditions applied in the box.

Figure 2 shows the force applied to pull the carbon nanotube, the graphene, and the nanocone from the cyclohexane layer into water. The force is expressed as a function of the center-of-mass (COM) position,  $z$ , of the carbon nanoparticle due to the pulling. The pull rate is  $10 \text{ nm ns}^{-1}$ . The force is initially small because the particles can aimlessly move within the hydrophobic (cyclohexane) environment at the specified pull rate. The pull force increases when the carbon particles approach the interface where the water–carbon interactions start to develop. When the carbons pass over the interface, the nearby bulk molecules are disturbed, causing the solvent–solvent interactions between the two solvents to enhance. As the particles move further on the  $z$  direction, they rotate in an appropriate direction to reduce the amount of hydrophobic interactions at their front. The particular orientation makes the force decrease.



**Figure 1.** Selected configurations from the pulling simulations of a carbon nanotube, a graphene, and a carbon nanocone, as they move from the cyclohexane layer into water. The snapshots correspond to the different  $z$  positions of the nanoparticles. The carbon atoms of the nanoparticles are shown with red spheres. Cyclohexane and water molecules are shown with black and light gray lines, respectively.

The advantage of the pulling simulations is that it allows creating a path of interest in a single, rapid simulation. For instance, a pulling simulation over only one nanosecond is sufficient to make the carbon nanoparticles travel a distance of 10 nm, penetrating the interface of cyclohexane and water. This is accomplished by setting an adaptive force and a pull rate ( $10 \text{ nm ns}^{-1}$ ) to help the nanoparticles overcome a free energy barrier and cross the interface. If it were not for the pull force, the interface would never be crossed, or it would be crossed with an appreciable hysteresis. Therefore, pulling simulations prepare the system for the presence of an interface, charting a path through which the carbon nanoparticles may pass. This path is statistically insignificant, since the particles can likely reach the same final state through infinite possible paths. In order to explore the relevant configuration space with statistical efficiency, we perform umbrella sampling simulations. Configurations such as those shown in Figure 1, picturing the position of the nanoparticle across the pulling path, become inputs to a sequence of individual umbrella simulations.



**Figure 2.** Pull force applied to carry the nanotube, the graphene, and the nanocone, from the cyclohexane layer into water, as a function of the position,  $z$ , of the nanoparticle. Lines show the moving average of the applied force over 2000 configurations. The vertical dashed-dot lines depict the positions of the nanoparticles in the configurations shown in Figure 1.

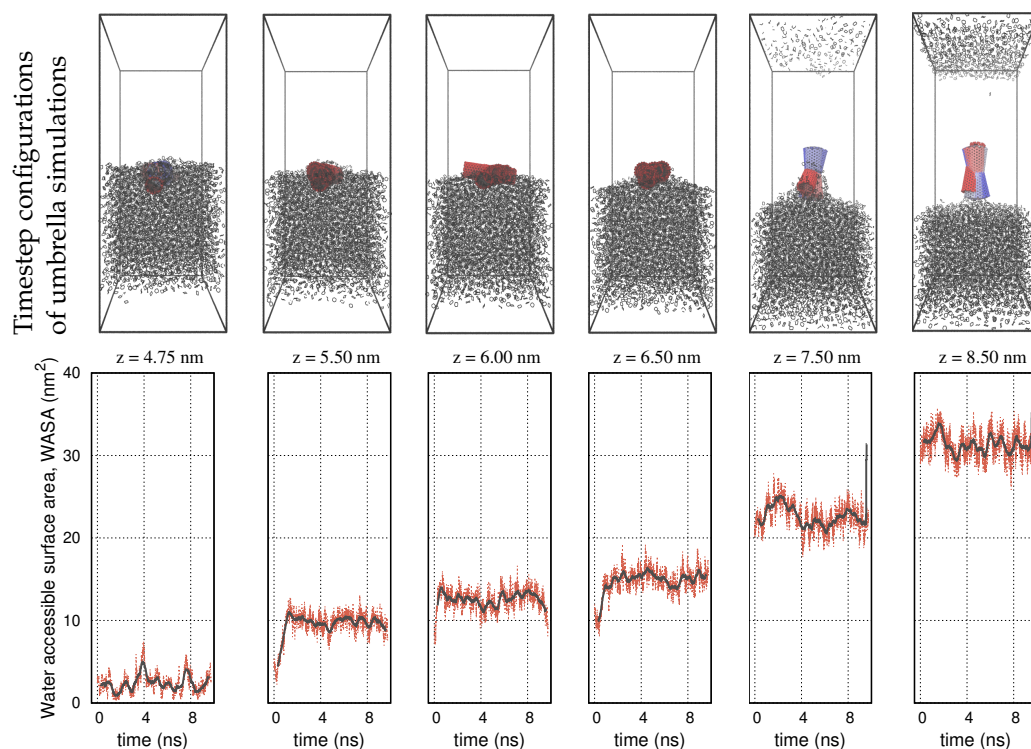


**Figure 3. Up:** Umbrella sampling configurations of the nanotube at different positions and timesteps near the interface of the solvents. The COM of the nanotube is set at the center of the box. The panels present 10 timestep configurations from each simulation. The nanotube is shown with a red–blue color palette. The colors correspond to the different timesteps. Cyclohexane molecules are shown with black lines. Water molecules are not shown for clarity. **Down:** Water-accessible surface area (WASA) of the nanotube during the umbrella sampling simulations. Black lines represent the moving averages of the WASA recordings over 100 sampled configurations.

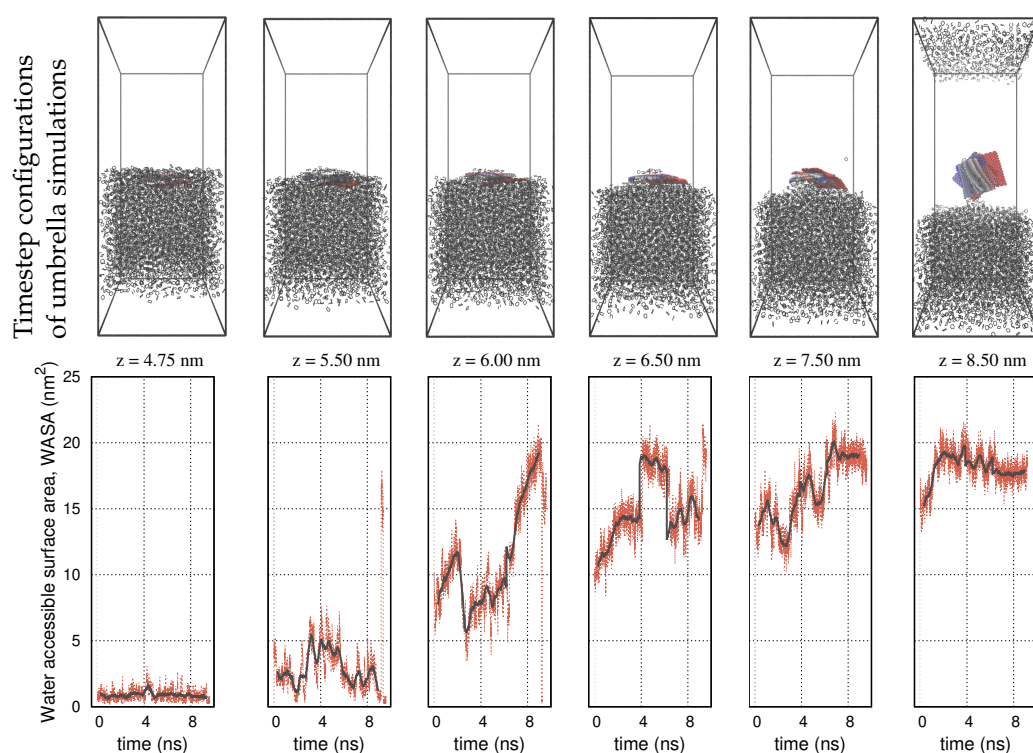


**Figure 4.** Up: Umbrella sampling configurations of the graphene at different positions and timesteps near the interface of the solvents. Down: Water-accessible surface area (WASA) of the graphene during the umbrella sampling simulations. We use the same color definitions as in Figure 3.

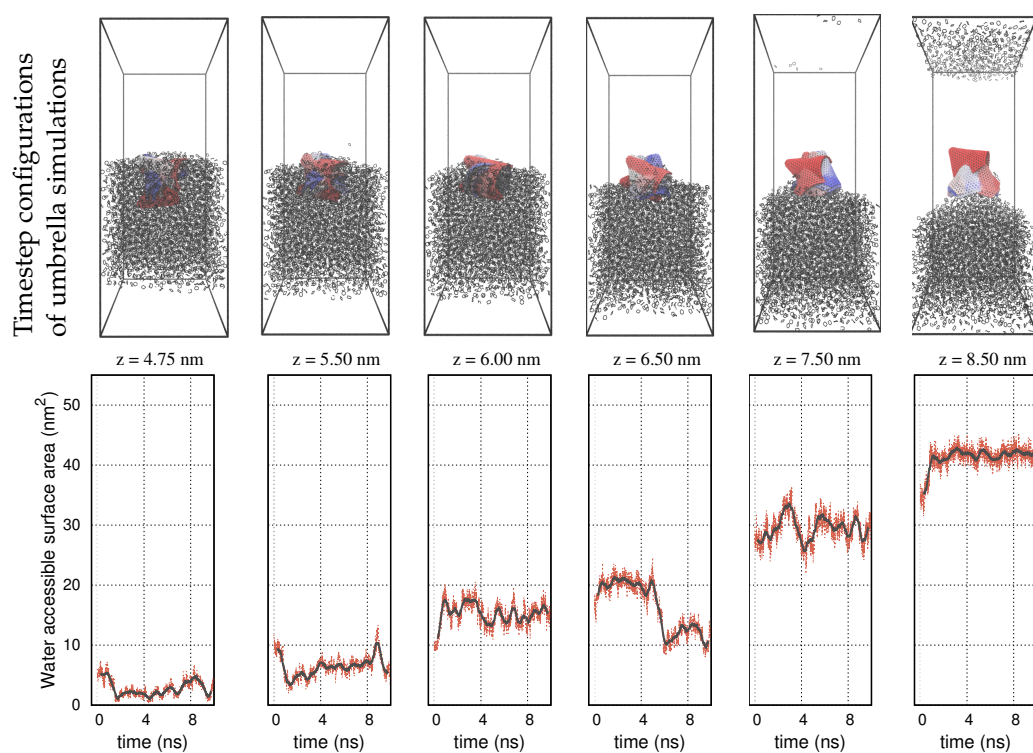


**Figure 5.** Up: Umbrella sampling configurations of the nanocone at different positions and timesteps near the interface of the solvents. Down: Water-accessible surface area (WASA) of the nanocone during the umbrella sampling simulations. We use the same color definitions as in Figure 3.



A selective set of umbrella sampling simulations performed on the carbon nanotube, the graphene, and the nanocone is shown in Figures 3–5, respectively. The carbon nanoparticles lay at certain positions,  $z$ , near the interface. In order to realize the configuration space of the umbrella sampling, we depict the carbon nanoparticles in 10 timestep configurations during the runs. In all representations, the timestep size is 1 ns and the simulations run over 10 ns. The COM of the carbon nanoparticles is centered in the box. We use a red–blue color palette to display the nanoparticles at the specified timesteps. The timestep configurations resemble those of the pulling simulation, as detailed in Figure 1. That is, in the cyclohexane layer, the carbon particles lay relatively planar to the interface, whereas inside the water environment, they rotate at a nearly normal direction to align with the  $z$  axis. Based on this outcome, we infer that the initial configurations, created by the pulling simulation, are indeed, the most frequently sampled configurations in the umbrella simulations. This confirms that the systems are well equilibrated during the NPT simulations, so that umbrella sampling is restrained in narrow energy distributions (umbrella windows), producing qualitatively similar configurations.

The panels on the second row in Figures 3–5 show the water-accessible surface area (WASA) of the carbon nanoparticles recorded during the same umbrella simulations as in the illustrations on the first row. WASA values present strong fluctuations with time, because the cyclohexane molecules are randomly exchanged with water on the fluid–wall interface during sampling. WASA is recorded for all the performed umbrella simulations. The time average of the WASA recordings expressed as a function of the COM position  $z$  of the carbon particles is shown in Figure 6. The nanoparticles are initially out of the range of water interactions, and therefore, their surface is inaccessible to water. When the carbons cross the interface, the cyclohexane molecules sweep gradually from the walls, leaving parts on the surface water accessible. Regarding the example of the graphene sheet, the top side of the sheet is wetted first, and the other side is wetted only after the graphene enters adequately the water layer and the sheet begins to rotate. Inside the water layer, the rotation of the carbon particles facilitates the fast rejection of the cyclohexane molecules from the walls. Presumably, when the particles are more aligned to the  $z$  axis, the hydrophobic interactions are better screened on both sides of the walls.

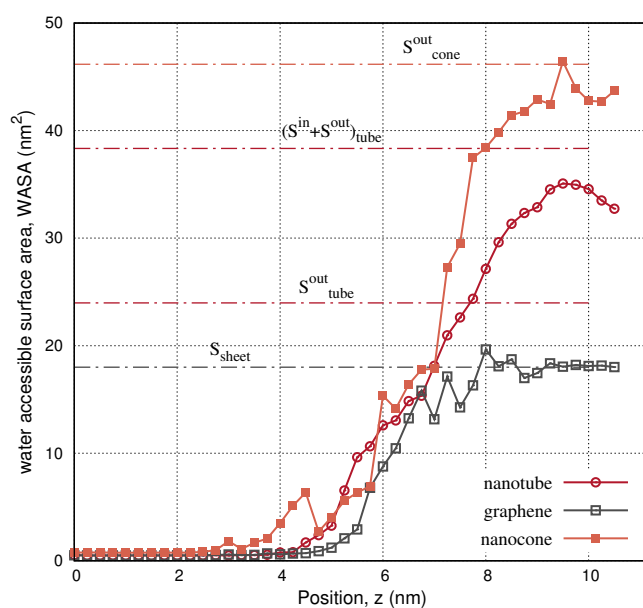


**Figure 6.** Water-accessible surface area (WASA) of the nanotube, the graphene, and the nanocone, as the nanoparticles move from the cyclohexane layer into water. The dashed–dot horizontal lines depict the external,  $S^{\text{out}}$ , and internal,  $S^{\text{in}}$ , geometric surface of the nanoparticles, as listed in Table 1.

In Figure 6, WASA values are compared to the geometrical surface of the nanoparticles, as listed in Table 1. In the case of the graphene, we detect a complete wetting of the



surface near the final state. There, the water-accessible surface area becomes twice the 3 nm square area of the sheet. This confirms that our calculations are consistent, because WASA is recorded using the same van der Waals radii in the atoms definition with the NPT simulations. On the other hand, WASA recordings of the nanotube show that a small amount of cyclohexane molecules is never rejected from the surface. Although the external surface of the nanotube ( $S^{out}$ ) becomes fully wet, cyclohexane molecules form a strict hydrophobic structure inside the cavity ( $S^{in}$ ), which is hardly disturbed by the water molecules entering the nanopore. Accordingly, WASA recordings of the nanocone show that this structure wets only the external surface. When the nanocone enters the aqueous environment, it shifts the conic tip upward, shielding the cyclohexane molecules behind the wall. Since cyclohexane is more attracted than water by the carbon sites, it creates a monolayer coverage over the concave wall, making the internal surface of the cone inaccessible to water. Notably, the water molecules restrict the cyclohexane structure to grow up to the thickness of a monolayer. We do not expect the cyclohexane to condense inside the conic pore, although it should be more concentrated near the apex, where the confinement is narrower.

In Figure 7, we present the potential mean force (PMF) of the carbon nanoparticles as a function of the COM position within the box. The plateau on the curves indicates that the particles are completely dissolved in water. This is achieved when the particles reach a distance larger than the cut-off from the cyclohexane–water interface. Lengthier and wider nanoparticles need to move further inside the water layer to dissolve. This explains why we set a larger height for the water layer than the cyclohexane when editing the box sizes. As the structures move, the nearby solvent molecules agitate. The agitations change the entropy and contribute to the system energy. The nanotube and the nanocone need considerably higher energy than the graphene to dissolve. It is because these structures create greater agitations to the ambient molecules than the graphene. It is also because the cone and the nanotube contain a nanopore. Cyclohexane molecules remain attached on the walls of the nanopore, even when these structures enter sufficiently the water layer. The adsorbed cyclohexane monolayer provides extra hydrophobic interactions in the water layer along with those counted on the interface of the solvents. The excess of the hydrophobic interactions increases the potential energy.

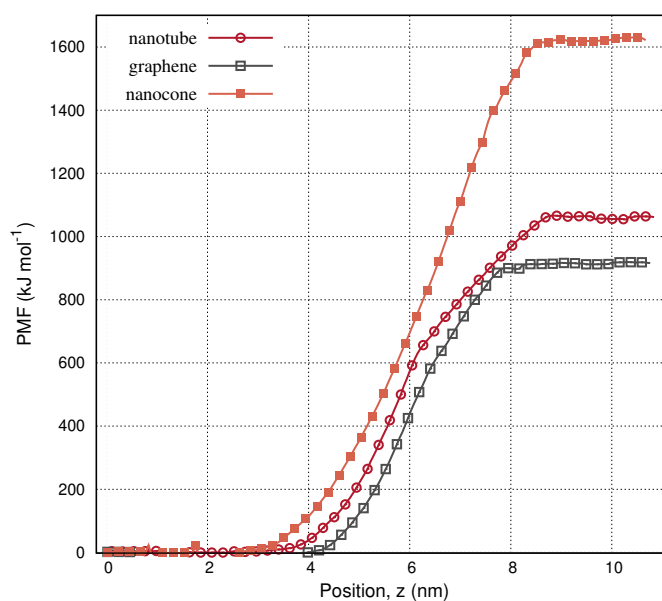


**Figure 7.** Potential of mean force (PMF) of the nanotube, the graphene, and the nanocone, as the nanoparticles move from the cyclohexane layer into water.

#### 4. Discussion

Realizing the properties of carbon sorbents in a solvated chemical environment requires first investigating the interfacial structures and interaction potentials with solvents having contradictory characteristics. For instance, cyclohexane and water differ in hydrophilicity and polarity. When a porous hydrophobic carbon is dispersed in cyclohexane, the cyclohexane molecules remain adsorbed inside the nanopores even after the sorbent is pushed into the aqueous layer. Inside the nanoconfinement, the hydrophobic molecules assume the role of pseudosurfactants, shielding the carbon wall from the interactions with the polar water molecules. This outcome, realized by umbrella sampling molecular dynamics, suggests an interesting direction for experimentation and may eventually help in the interpretation of the relevant results. Taking advantage of the simplicity of the carbon surface, we establish a lower bound on the sampling necessary to simulate more complex low-dimensional materials such as functionalized graphenes, metal oxides, and metal–organic nanosheets (MONs). This work is a precursor of an ongoing large simulation study of the binding affinities of these solids in environments with conjugated solvent molecules such as surfactants, ionic liquids, and lipid bilayers.

#### 5. Conclusions

We performed umbrella sampling molecular dynamics to simulate three carbon nanoparticles with different shapes crossing the interface of cyclohexane and water. We used a pull force to direct the nanoparticles from the cyclohexane layer to water with the scope to create the initial configurations for the umbrella simulations. Inside the water layer, the nanoparticles aligned with the pulling direction. The particular orientation facilitated the rejection of the cyclohexane molecules from the external walls of the nanoparticles. On the contrary, the surface inside nanoconfinements remained dry. This was because water circumvented the hydrophobic interactions inside the nanopores. We demonstrated that a carbon nanotube and a nanocone needed higher energy than a graphene nanosheet to cross the cyclohexane–water interface. This was attributed to the agitations of the solvent phases due to the movement of the large nanoparticles. It was also attributed to the nanoconfined cyclohexane molecules, which remained adsorbed inside the water layer and contributed to the potential energy.

**Funding:** This research received no external funding.

**Data Availability Statement:** Data can be available in Gromacs filetypes such as gro, xvg, xtc, dat, and txt. Also codes are available in .sh, .py and pl.

**Conflicts of Interest:** The author declares no conflict of interest.

#### References

1. Cracknell, R.F.; Gubbins, K.E.; Maddox, M.; Nicholson, D. Modeling Fluid Behavior in Well-Characterized Porous Materials. *Accounts Chem. Res.* **1995**, *28*, 281–288. [\[CrossRef\]](#)
2. Bojan, M.J.; van Slooten, R.; Steele, W. Computer Simulation Studies of the Storage of Methane in Microporous Carbons. *Sep. Sci. Technol.* **1992**, *27*, 1837–1856. [\[CrossRef\]](#)
3. Bojan, M.J.; Vernov, A.V.; Steele, W.A. Simulation studies of adsorption in rough-walled cylindrical pores. *Langmuir* **1992**, *8*, 901–908. [\[CrossRef\]](#)
4. Maddox, M.W.; Gubbins, K.E. Molecular simulation of fluid adsorption in buckytubes and MCM-41. *Int. J. Thermophys.* **1994**, *15*, 1115–1123. [\[CrossRef\]](#)
5. Sweatman, M.B.; Quirke, N. Characterization of Porous Materials by Gas Adsorption Comparison of Nitrogen at 77 K and Carbon Dioxide at 298 K for Activated Carbon. *Langmuir* **2001**, *17*, 5011–5020. [\[CrossRef\]](#)
6. Kowalczyk, P.; Gun'ko, V.M.; Terzyk, A.P.; Gauden, P.A.; Rong, H.; Ryu, Z.; Do, D.D. The comparative characterization of structural heterogeneity of mesoporous activated carbon fibers (ACFs). *Appl. Surf. Sci.* **2003**, *206*, 67–77. [\[CrossRef\]](#)
7. Gotzias, A.; Charalambopoulou, G.; Steriotis, T. On the orientation of N<sub>2</sub> and CO<sub>2</sub> molecules adsorbed in slit pore models with oxidised graphitic surface. *Mol. Simul.* **2016**, *42*, 186–195. [\[CrossRef\]](#)
8. Gotzias, A.; Sapalidis, A. Pulling Simulations and Hydrogen Sorption Modelling on Carbon Nanotube Bundles. *C* **2020**, *6*. [\[CrossRef\]](#)

9. Neimark, A.V.; Lin, Y.; Ravikovitch, P.I.; Thommes, M. Quenched solid density functional theory and pore size analysis of micro-mesoporous carbons. *Carbon* **2009**, *47*, 1617–1628. [[CrossRef](#)]
10. Thomson, K.T.; Gubbins, K.E. Modeling Structural Morphology of Microporous Carbons by Reverse Monte Carlo. *Langmuir* **2000**, *16*, 5761–5773. [[CrossRef](#)]
11. Gotzias, A. Calculating adsorption isotherms using Lennard Jones particle density distributions. *J. Phys. Condens. Matter* **2019**, *31*, 435901. [[CrossRef](#)]
12. Denoyel, R.; Fernandez-Colinas, J.; Grillet, Y.; Rouquerol, J. Assessment of the surface area and microporosity of activated charcoals from immersion calorimetry and nitrogen adsorption data. *Langmuir* **1993**, *9*, 515–518. [[CrossRef](#)]
13. Silvestre-Albero, J.; Gómez de Salazar, C.; Sepúlveda-Escribano, A.; Rodríguez-Reinoso, F. Characterization of microporous solids by immersion calorimetry. *Colloids Surfaces Physicochem. Eng. Asp.* **2001**, *187–188*, 151–165. [[CrossRef](#)]
14. Dziaćko, R.A.; Janicek, B.E.; Karten, J.L.; Harris, K.A.; Gibson, M.M.; Crowther, A.C. Solvent-Mediated Chemical Hole Doping of Graphene by Iodine. *J. Phys. Chem. C* **2020**, *124*, 3827–3834. [[CrossRef](#)]
15. Hernandez, Y.; Nicolosi, V.; Lotya, M.; Blighe, F.M.; Sun, Z.; De, S.; McGovern, I.T.; Holland, B.; Byrne, M.; Gun'Ko, Y.K.; et al. High-yield production of graphene by liquid-phase exfoliation of graphite. *Nat. Nanotechnol.* **2008**, *3*, 563–568. [[CrossRef](#)] [[PubMed](#)]
16. Coleman, J.N.; Lotya, M.; O'Neill, A.; Bergin, S.D.; King, P.J.; Khan, U.; Young, K.; Gaucher, A.; De, S.; Smith, R.J.; et al. Two-Dimensional Nanosheets Produced by Liquid Exfoliation of Layered Materials. *Science* **2011**, *331*, 568–571. [[CrossRef](#)]
17. Tang, H.; Zhao, Y.; Yang, X.; Liu, D.; Shan, S.; Cui, F.; Xing, B. Understanding the pH-dependent adsorption of ionizable compounds on graphene oxide using molecular dynamics simulations. *Environ. Sci. Nano* **2017**, *4*, 1935–1943. [[CrossRef](#)]
18. Lemkul, J.A.; Allen, W.J.; Bevan, D.R. Practical Considerations for Building GROMOS-Compatible Small-Molecule Topologies. *J. Chem. Inf. Model.* **2010**, *50*, 2221–2235. [[CrossRef](#)]
19. Hinkle, K.R.; Phelan, F.R. Solvation of Carbon Nanoparticles in Water/Alcohol Mixtures: Using Molecular Simulation To Probe Energetics, Structure, and Dynamics. *J. Phys. Chem. C* **2017**, *121*, 22926–22938. [[CrossRef](#)] [[PubMed](#)]
20. Schneemilch, M.; Quirke, N. Free energy of adhesion of lipid bilayers on silica surfaces. *J. Chem. Phys.* **2018**, *148*, 194704. [[CrossRef](#)] [[PubMed](#)]
21. Aragonés, J.L.; Noya, E.G.; Valeriani, C.; Vega, C. Free energy calculations for molecular solids using GROMACS. *J. Chem. Phys.* **2013**, *139*, 034104. [[CrossRef](#)] [[PubMed](#)]
22. Perthold, J.W.; Petrov, D.; Oostenbrink, C. Toward Automated Free Energy Calculation with Accelerated Enveloping Distribution Sampling (A-EDS). *J. Chem. Inf. Model.* **2020**, *60*, 5395–5406. [[CrossRef](#)] [[PubMed](#)]
23. Gotzias, A. Binding Free Energy Calculations of Bilayer Graphenes Using Molecular Dynamics. *J. Chem. Inf. Model.* **2021**, *61*, 1164–1171. [[CrossRef](#)] [[PubMed](#)]
24. Gotzias, A.; Tocci, E.; Sapalidis, A. On the Consistency of the Exfoliation Free Energy of Graphenes by Molecular Simulations. *Int. J. Mol. Sci.* **2021**, *22*, 8291. [[CrossRef](#)] [[PubMed](#)]
25. Christ, C.D.; van Gunsteren, W.F. Multiple free energies from a single simulation: Extending enveloping distribution sampling to nonoverlapping phase-space distributions. *J. Chem. Phys.* **2008**, *128*, 174112. [[CrossRef](#)]
26. Tang, X.; Koenig, P.H.; Larson, R.G. Molecular Dynamics Simulations of Sodium Dodecyl Sulfate Micelles in Water—The Effect of the Force Field. *J. Phys. Chem. B* **2014**, *118*, 3864–3880. [[CrossRef](#)] [[PubMed](#)]
27. Bohlén, M.; Bolton, K. Molecular dynamics studies of the influence of single wall carbon nanotubes on the mechanical properties of Poly(vinylidene fluoride). *Comput. Mater. Sci.* **2013**, *68*, 73–80. [[CrossRef](#)]
28. Bandosz, T.; Biggs, M.; Gubbins, K.; Hattori, Y.; Liyama, T.; Kaneko, K.; Pikunic, J.; Thomson, K. Molecular models of porous carbons. In *Chemistry & Physics of Carbon*, 1st ed.; Radovic, L., Ed.; CRC Press: Boca Raton, FL, USA, 2003; pp. 41–218. [[CrossRef](#)]
29. Bock, H.; Gubbins, K.E.; Pikunic, J. Chapter Five—Models of Porous Carbons. In *Adsorption by Carbons*; Elsevier: Amsterdam, The Netherlands, 2008; pp. 103–132.
30. Gao, Y.; Maruyama, M.; Okada, S. Influence of interlayer stacking arrangements on carrier accumulation in bilayer graphene field effect transistors. *Appl. Phys. Express* **2020**, *13*, 065006. [[CrossRef](#)]
31. Vögele, M.; Köfinger, J.; Hummer, G. Molecular dynamics simulations of carbon nanotube porins in lipid bilayers. *Faraday Discuss.* **2018**, *209*, 341–358. [[CrossRef](#)]
32. Puigpelat, E.; Ignés-Mullol, J.; Sagués, F.; Reigada, R. Interaction of Graphene Nanoparticles and Lipid Membranes Displaying Different Liquid Orderings: A Molecular Dynamics Study. *Langmuir* **2019**, *35*, 16661–16668. [[CrossRef](#)]
33. Arjmandi-Tash, H.; Lima, L.M.C.; A. Belyaeva, L.; Mukhina, T.; Fragneto, G.; Kros, A.; Charitat, T.; Schneider, G.F. Encapsulation of Graphene in the Hydrophobic Core of a Lipid Bilayer. *Langmuir* **2020**, *36*, 14478–14482. [[CrossRef](#)] [[PubMed](#)]
34. Guo, R.; Mao, J.; Yan, L.T. Computer simulation of cell entry of graphene nanosheet. *Biomaterials* **2013**, *34*, 4296–4301. [[CrossRef](#)] [[PubMed](#)]
35. Fedel, M. Hemocompatibility of Carbon Nanostructures. *C* **2020**, *6*, 12. [[CrossRef](#)]
36. Gotzias, A. Injecting Carbon Nanostructures in Living Cells. In Proceedings of the Workshops of the 11th EETN Conference on Artificial Intelligence 2020 (SETN2020 Workshops), Athens, Greece, 2–4 September 2020.
37. Kordzadeh, A.; Amjad-Iranagh, S.; Zarif, M.; Modarress, H. Adsorption and encapsulation of the drug doxorubicin on covalent functionalized carbon nanotubes: A scrutinized study by using molecular dynamics simulation and quantum mechanics calculation. *J. Mol. Graph. Model.* **2019**, *88*, 11–22. [[CrossRef](#)]

38. Narjabadifam, A.; Vakili-Tahami, F.; Zehsaz, M. Modal analysis of multi-walled carbon nanocones using molecular dynamics simulation. *Comput. Mater. Sci.* **2017**, *137*, 55–66. [CrossRef]
39. Wohner, N.; Lam, P.; Sattler, K. Energetic stability of graphene nanoflakes and nanocones. *Carbon* **2014**, *67*, 721–735. [CrossRef]
40. Karataraki, G.; Sapalidis, A.; Tocci, E.; Gotzias, A. Molecular Dynamics of Water Embedded Carbon Nanocones: Surface Waves Observation. *Computation* **2019**, *7*, 50. [CrossRef]
41. Ge, M.; Sattler, K. Observation of fullerene cones. *Chem. Phys. Lett.* **1994**, *220*, 192–196. [CrossRef]
42. Krishnan, A.; Dujardin, E.; Treacy, M.M.J.; Hugdahl, J.; Lynam, S.; Ebbesen, T.W. Graphitic cones and the nucleation of curved carbon surfaces. *Nature* **1997**, *388*, 451–454. [CrossRef]
43. Naess, S.N.; Elgsaeter, A.; Helgesen, G.; Knudsen, K.D. Carbon nanocones: Wall structure and morphology. *Sci. Technol. Adv. Mater.* **2009**, *10*, 065002. [CrossRef]
44. Heiberg-Andersen, H.; Skjeltorp, A.T. Stability of Conjugated Carbon Nanocones. *J. Math. Chem.* **2005**, *38*, 589–604. [CrossRef]
45. Bultheel, A.; Ori, O. Topological modeling of 1-Pentagon carbon nanocones—Topological efficiency and magic sizes. *Fullerenes Nanotub. Carbon Nanostruct.* **2018**, *26*, 291–302. [CrossRef]
46. Nazeer, W.; Farooq, A.; Younas, M.; Munir, M.; Kang, S.M. On Molecular Descriptors of Carbon Nanocones. *Biomolecules* **2018**, *8*, 92. [CrossRef] [PubMed]
47. Apriliyanto, Y.B.; Battaglia, S.; Evangelisti, S.; Faginas-Lago, N.; Leininger, T.; Lombardi, A. Toward a Generalized Hückel Rule: The Electronic Structure of Carbon Nanocones. *J. Phys. Chem. A* **2021**, *125*, 9819–9825. [CrossRef] [PubMed]
48. Gotzias, A.; Heiberg-Andersen, H.; Kainourgiakis, M.; Steriotis, T. A grand canonical Monte Carlo study of hydrogen adsorption in carbon nanohorns and nanocones at 77K. *Carbon* **2011**, *49*, 2715–2724. [CrossRef]
49. Gotzias, A.; Heiberg-Andersen, H.; Kainourgiakis, M.; Steriotis, T. Grand canonical Monte Carlo simulations of hydrogen adsorption in carbon cones. *Appl. Surf. Sci.* **2010**, *256*, 5226–5231. [CrossRef]
50. Ulloa, P.; Pacheco, M.; Latgé, A. Optical properties of graphene nanocones under electric and magnetic fields. *J. Phys. Condens. Matter* **2017**, *29*, 455304. [CrossRef]
51. Chen, I.C.; Chen, L.H.; Ye, X.R.; Daraio, C.; Jin, S.; Orme, C.A.; Quist, A.; Lal, R. Extremely sharp carbon nanocone probes for atomic force microscopy imaging. *Appl. Phys. Lett.* **2006**, *88*, 153102. [CrossRef]
52. Furmaniak, S.; Gauden, P.A.; Patrykiewicz, A.; Miśkiewicz, R.; Kowalczyk, P. Carbon Nanohorns as Reaction Nanochambers—A Systematic Monte Carlo Study. *Sci. Rep.* **2018**, *8*, 15407. [CrossRef]
53. Jarzynski, C. Equilibrium free-energy differences from nonequilibrium measurements: A master-equation approach. *Phys. Rev. E* **1997**, *56*, 5018–5035. [CrossRef]
54. Lemkul, J.A.; Bevan, D.R. Assessing the Stability of Alzheimer’s Amyloid Protofibrils Using Molecular Dynamics. *J. Phys. Chem. B* **2010**, *114*, 1652–1660. [CrossRef] [PubMed]
55. Minoia, A.; Chen, L.; Beljonne, D.; Lazzaroni, R. Molecular modeling study of the structure and stability of polymer/carbon nanotube interfaces. *Polymer* **2012**, *53*, 5480–5490. [CrossRef]
56. Available online: <http://chembytes.wikidot.com> (accessed on 25 January 2022).
57. Kumar, S.; Rosenberg, J.M.; Bouzida, D.; Swendsen, R.H.; Kollman, P.A. The weighted histogram analysis method for free-energy calculations on biomolecules. I. The method. *J. Comput. Chem.* **1992**, *13*, 1011–1021. [CrossRef]
58. doi: 10.1002/jcc.540160303 Eisenhaber, F.; Lijnzaad, P.; Argos, P.; Sander, C.; Scharf, M. The double cubic lattice method: Efficient approaches to numerical integration of surface area and volume and to dot surface contouring of molecular assemblies. *J. Comput. Chem.* **1995**, *16*, 273–284. [CrossRef]
59. Bondi, A. van der Waals Volumes and Radii. *J. Phys. Chem.* **1964**, *68*, 441–451. [CrossRef]